A paper that is presented in Open Access format

First author*[1]

[1]Department of Civil and Environmental Engineering, Norwegian University of Science and Technology (NTNU), 7491 Trondheim, Norway

, 2020, **83** , pp. 905-916.
DOI: http://dx.doi.org/10.1002/gghh.ppplll20122

Abstract

The study of wave interaction with porous structures is essential as coastal structures are often porous in nature due to their prominent energy dissipation characteristics. The present work is focused on the numerical modeling of wave interaction with submerged porous structures which are often classified as reef breakwaters and low crested structures. Numerical modeling of wave interaction with porous structures is considered to be a challenge for researchers due to the complexities associated with it. The present study numerically investigates the wave interaction process through the porous media by representing the porous media using Volume averaged Reynolds Averaged Navier–Stokes (VRANS) equations. For the study, an open-source RANS based CFD tool, REEF3D has been used for numerical modeling. The study also consists of experiments which are used for validating the numerical model. The numerical results for the free surface elevation and the hydrodynamic pressure are compared with the experimental measurements and found to be in good agreement. The numerical study is extended to different crest widths of the structure and varying wave parameters to investigate the effects of various dimensionless parameters affecting wave transmission. The frequency-domain analysis is performed to investigate the energy distribution of the incident and transmitted waves. Finally, the utility of numerical model adopting VRANS equations has been demonstrated for climate change mitigation studies. This has been carried out by studying the effects of pressure reduction on a vertical seawall due to the presence of a porous reef breakwater in the seaside. Pressure reduction up to 32% is calculated due to the presence of the porous structure in front of the seawall and this demonstrates the application of reef breakwaters for coastal resilience studies. Such investigations are useful in protecting the existing coastal structures prone to severe wave conditions exceeding the design limits. .

Keywords: Climate change mitigation, Low crested structures, Porous media, Reef breakwaters, REEF3D, VRANS modeling, Wave attenuation.

---

*Corresponding author,author@ntnu.no

1 Introduction

Low crested structures such as reef breakwaters are increasingly adopted for the protection of coasts. These structures are often associated with soft engineering approaches in coastal engineering as these structures are submerged near the coast and wave attenuation is achieved off the coast. Further, permeable porous structures are frequently preferred to impermeable structures owing to its energy absorbing/ dissipative characteristics (Garcia et al. 2004, Jensen et al. 2014, Lin and Karunarathna 2007). Conventionally, the design of coastal structures such as breakwaters, groins, seawalls is carried out based on physical model studies to determine the hydrodynamic characteristics of the structures, which involves a large amount of resources and time. With improved computational facilities, numerical simulations are increasingly becoming popular to study wave structure interaction and are increasingly employed in the field of coastal engineering. The present research focusses on the numerical representation of the hydrodynamics in and around a porous structure subjected to wave action. This involves the accurate simulation of free surface elevation and the pressure field in the vicinity of the porous structure. Wave attenuation is the primary function of these low crested structures and hence the accurate simulation of the free surface is very essential. Further, the hydrodynamic characteristics such as transmission and reflection coefficients are dependent on the wave elevation which emphasizes the need for such studies. These aspects have also been highlighted by past investigators such as Dattatri et al. (1978), Garcia et al. (2004), Seelig (1980), Seabrook and Hall (1998), van der Meer et al. (2005). Modeling the hydrodynamic pressures over and inside the porous media is the other facet that the present work focusses on. The importance of simulation of the pressure field in the porous media has also been discussed in the work of Garcia et al. (2004). The simulation of the pressure field on the outer periphery of the porous media is crucial as it relates to the forces acting on it. This provides information concerning the structural stability which can be applied to determine the size of the armor units required for a given wave climate. In addition, the simulation of pressure inside the porous media provides insights into the pore water pressure and the amount of damping offered by the porous media. Further, the estimation transmission coefficient is the primary factor considered for the design of structures for coastal defense. With the development of computational tools capable of simulating the wave interaction with porous structures, the design of the coastal structures will become handy. Numerical simulation of flow through porous structures using friction coefficients can be noticed from the work of van Gent (1995). Liu et al. (1999) have done extensive research on modeling wave interaction with porous structures. They adopted the Volume Averaged RANS equations to account for the flow inside the porous media. A similar approach has also been used by van Gent (1995) where resistance coefficients are used to bring in the effect of porous media. In the past, Lara et al. (2006) have applied RANS modeling to represent random wave interaction with submerged permeable structures. The resistance coefficients are usually determined from physical model experiments as a part of calibrating the numerical model (Jensen et al. 2014). This is essential to calibrate the model in order to account for the physical processes taking place during the flow through the porous media. It is worth mentioning the work of Higuera

Postprint, published in , doi:http://dx.doi.org/10.1002/gghh.pppll20122

et al. (2013 a,b) where the effects of wave interaction with porous structures have been studied in three dimensions. The author describes the importance of turbulence modeling for such exercise. The state of art review by Losada et al. (2016) clearly states the need for such studies involving numerical simulation of wave interaction with submerged structures. This is very important as the use of porous materials in coastal engineering is inevitable and proper representation of the hydrodynamics around the porous structure is of utmost significance. Further, the influence of the material properties such as porosity, stone size, material gradation, of the porous media, affecting the flow damping is not well understood as pointer out by Losada et al. (2016). In the present study, an open-source RANS code REEF3D has been adopted to study the effect of wave interaction with a submerged porous structure. The numerical model, REEF3D, has been used in the past for studies pertaining to wave-structure interaction (Aggarwal et al. 2019; Ahmad et al. 2019). In the present work, the porous structure is modeled using the VRANS approach (Sasikumar et. al. 2018). The numerical model adopting VRANS equations requires calibration of resistance coefficients and hence, the experimental measurements involving wave interaction with submerged porous structure is used for the calibration of the numerical model. The experimental work has been conducted in the shallow water wave flume of the Department of Ocean Engineering, Indian Institute of Technology Madras, India and the major results pertaining to the performance characteristics of the porous reef breakwater such as wave transmission and the reflection has been published (Srineash and Murali 2019). The study also investigates the influence of crest width and the wave parameters affecting the wave transmission. The comparison of experimental measurements with the numerical simulations is focused on the wave elevations and hydrodynamic pressures. The comparison of experiments with the numerical simulations is carried out with three crest widths. Further, the investigation has been carried forward to study the wave transmission process over the porous media. The effects of the energy distribution of the incident and transmitted waves are also examined in the frequency domain using spectral analysis. Recent times, a great deal of research is being focused to counter the effects of climate change issues such as the sea-level rise and frequent occurrence of storms (Sasikumar et al. 2018 and Srineash and Murali 2019). In order to demonstrate the ability of the open-source CFD tool using VRANS equations for practical applications, a case study is taken up to study the effect of reef breakwater placed in tandem to a vertical seawall. The use of such reef breakwaters is looked into as a way of protecting the existing maritime structures against extreme scenarios (Pilarczyk 2003). The use of reef breakwaters in tandem becomes a viable solution when the existing structure is prone to more severe wave conditions than considered during the design. This study on the effects of pressure reduction on the vertical seawall defended by a porous reef breakwater on its seaside has been carried out numerically after validating the numerical model with experimental results for porous structures. This extends the investigation of the wave-porous structure interaction to an innovative solution for strengthening coastal protection structures for more frequent harsh weather events of higher magnitudes than expected during design and construction.

2 Methods

The following section discusses the various variables and parameters considered for the numerical investigation. The details pertaining to the numerical modeling aspects of the wave

interaction with porous structure is brought out below.

2.1 Variables and Parameters

The following variables and parameters are considered essential in the study involving wave interaction with the submerged porous structures (Figure 1). The depth of submergence of the structure (d') and the incident wave height (H) are considered to be important variables affecting the wave transmission over submerged structures. This is represented in the nondimensional form as the relative depth of submergence (d'/H). The relative depth of submergence (d'/H) is reported to be the primary parameter in governing the transmission characteristics of submerged low crested structures (Ahrens 1987, Briganti et al. 2003, d'Angremond et al. 1996, Tanaka 1976, van der Meer and Daemen 1994, van der Meer et al. 2005) and hence in the present study, the transmission coefficient (K_t) is studied as a function of relative depth of submergence (d'/H). Where the transmission coefficient is defined as the ratio of the transmitted wave height (H_t) to the incident wave height (H). The transmitted wave height is obtained from the wave record pertaining to transmitted wave gauge (η_3) which is located on the shoreward side of the porous structure (Figure 1). The incident wave height is defined as the wave height that would have occurred in the location η_3, without the presence of the porous structure (Ahrens 1984, Ahrens 1987, van der Meer et al. 2005). This approach where the incident wave height is ascertained without the presence of the structure in the wave tank is considered to result in reliable incident wave height measurements (van der Meer et al. 2005). This method is recommended for wave tank tests involving breaking wave conditions (van der Meer et al. 2005). This approach also has the benefit of eliminating the energy losses between the incident and the transmitted wave gauges (Ahrens 1984, Ahrens 1987) which would occur in the conventional approaches (two probe / three probe approach). This is because, in the case of conventional approaches, multiple probes are positioned at the seaward side of the structure to resolve the wave elevation measurements into the incident and reflected components. Hence there is a possibility of energy loss that may occur as the locations of the incident and transmitted wave gauges are different. Further, physical variables such as the crest width of the structure (B), the wavelength (L) and depth (d) at the toe of the structure are represented nondimensionally as crest width ratio (B/d), relative crest width (B/L) and relative water depth (d/L). The relative crest width (B/L) is also associated with the wave transmission (Sasikumar et al. 2018, Tanaka 1976). The submergence ratio (d'/d) is maintained constant throughout the study with a value of 0.34. The range of variables and non-dimensional parameters considered in the study is presented in Table 1 and 2 respectively. The study consists of wave periods (T) ranging from 1.4 – 2.8 s and this can be understood from Table 1. Further, in the investigations pertaining to the effects of reef breakwater placed in tandem to the vertical seawall, an additional variable called pool length, l_p, is considered.

2.2 Numerical Modeling

To study the effect of wave interaction with porous structures, a numerical wave tank is modeled using the open-source CFD code REEF3D (Bihs et al. 2016). The wave field in the Numerical Wave Tank (NWT) is described using RANS equations. The model has been previously used to investigate complex wave-structure interaction with impermeable submerged structures (Kamath et al. 2017, Sasikumar et al. 2019, Srineash and Murali, 2018) and has

Variable	Definition	Range	Unit
T	Wave period	1.4 – 2.8	s
H	Wave height	0.02 – 0-05	m
d'	Depth of submergence	0.1	m
B	Crest width	0.30 – 0.90	m
L	Wavelength	2.14 – 4.68	m
l_p	Relative pool length	1 – 3	m

Table 1: Range of variables considered in the study

Non-dimensional parameter	Definition	Range
d/L	Relative water depth	0.064 – 0.14
d'/H	Relative depth of submergence	0.91 – 2.55
B/d	Crest width ratio	1 – 3
B/L	Relative crest width	0.14 – 0.42
d'/d	Submergence ratio	0.34
H/d	Relative pool height	0.13 – 0.22
l_p/L	Relative pool length	0.47 – 1.40

Table 2: Range of Non-dimensional parameters considered in the study

provided reliable results. Proper representation of the flow taking place inside the porous media is essential to replicate the physical behavior of wave interaction with porous structure, taken up in the present study. The approaches used to model the flow taking place within the porous media can be categorized as macroscopic and microscopic approaches (Losada et al., 2016). The macroscopic approach involves special averaging of flow taking place inside the porous media and neglecting other properties of the porous media. This macroscopic approach involves the coupling of two flow models, one representing the flow taking place inside the porous media and others to represent the flow outside the porous media. This approach involves calibration of the model to get constants which will be specific to the material properties of porous media considered. The second approach to model the flow within the porous media is the microscopic approach, where, the real features of the porous media such as the internal geometry, gradation, etc., are represented. This approach is computationally expensive and not practical in the field of coastal engineering as the pore-scale resolution of the porous media is not essential. The other disadvantage of the microscopic approach is that it is restricted to smaller domains as it requires fine mesh description. However, this method is being used oil and gas industry for multiphase flow simulations (Losada et al., 2016). In the present study, a macroscopic approach has been adopted to represent the porous media by Volume averaging RANS equations. This approach is popular in the field of coastal engineering for such applications.

2.3 VRANS equations

The porous media in the NWT is modelled using VRANS approach which can be categorized as macroscopic approach. The effect of porosity is represented in the study by means of volume averaging the RANS equations. Such a process is carried out by dividing the momentum

equation with the porosity of the porous media. The momentum equation of the porous media on volume averaging is shown in Eq. 1.

$$(1+C_m)\frac{\partial}{\partial t}\left(\frac{\langle\bar{u}_i\rangle}{n}\right)+\frac{1}{n}\frac{\partial}{\partial x_j}\left(\frac{\langle\bar{u}_i\rangle\langle\bar{u}_j\rangle}{n}\right)=-\frac{1}{\rho}\frac{\partial\langle\bar{P}^f\rangle}{\partial x_j}+\frac{1}{n}\frac{\partial}{\partial x_j}\nu\left(\frac{\partial\langle\bar{u}_i\rangle}{\partial x_j}+\frac{\partial\langle\bar{u}_j\rangle}{\partial x_i}\right)+g_j+F_i \quad (1)$$

Where, $\langle\rangle$ represents the volume averaging over the entire control volume and $\langle\ \rangle^f$ denotes the intrinsic volume average over the pore volume alone; hence the intrinsic pore pressure is expressed as $\langle\bar{P}\rangle^f$. The term $\langle\bar{u_i}\rangle$ in the Eq. 1 is the ensemble velocity averaged over the entire volume including the porous media and it is also known as filter velocity (Jensen et al. 2014). The porosity n is defined as volume of voids to the total volume; g is the acceleration due to gravity; ρ is the density; ν is the kinematic viscosity and P is the pressure. One may note from Eq. 1 that the filter velocities are divided by the porosity of the porous media in order to maintain the appropriate momentum. This process facilitates the use of filter velocities in place of pore velocities. The viscous term (ν) in the Eq. 1 becomes important to capture the interaction taking place in the interfacial region of the porous media (Liu et al. 1999). The resistance forces (linear, nonlinear and inertial forces) encountered due to the presence of the porous media is modeled using the term F_i. The extended Darcy-Forcheimmer equation is used to model the linear and nonlinear forces as shown in Eq. 2.

$$F_i=-a\rho\langle\bar{u}_i\rangle-b\rho\sqrt{(\bar{u}_j)(\bar{u}_j)(\bar{u}_i)} \quad (2)$$

The coefficients a and b in Eq. 2 are resistance coefficients which have to be determined. The relation between the resistance coefficients (a and b) with the properties such as porosity (n), density (ρ), median stone size (d_{50}), kinematic viscosity (ν) is described in the Eqs. 3 and 4 as described below.

$$a=\alpha\left(\frac{(1-n)^2}{n^3}\right)\left(\frac{\nu}{\rho\ d_{50}^2}\right) \quad (3)$$

$$b=\beta\left(1+\frac{7.5}{KC}\right)\left(\frac{1-n}{n^3}\right)\left(\frac{1}{d_{50}}\right) \quad (4)$$

The terms α and β in Eqs. 3 and 4 respectively are empirical coefficients which have to be determined by calibration, KC is the Keulegan-Carpenter number (KC = $u_0\ T/n\ d_{50}$), where u_0 is the maximum oscillatory velocity. The coefficients α and β may vary depending on the median stone size, porosity, stone shape, and other factors and hence calibration of these coefficients is essential to model the fluid interaction with porous media appropriately.

$$C_m=\gamma_p\frac{1-n}{n} \quad (5)$$

The term C_m is used in the Eq. 1 to represent the added mass effect in the porous media. The relation of the added mass coefficient with respect to porosity is expressed as given in Eq. 5 as suggested by van Gent (1995). The term γ_p in the Eq. 5 is an empirical coefficient taking a value of 0.34. More details pertaining to the derivation of VRANS equations may be found from the work is Jensen et al. (2014).

2.4 Turbulence Modeling in VRANS Approach

Turbulence modeling is considered to be very essential in relation to wave structure interaction studies involving porous structure/ media. Accurate modeling of flow taking place in and around the porous media requires turbulence modeling (Higuera et al., 2013a) as the flow around the porous media is often energetic with dissipation taking place due to the effects of turbulence. In the work of Jensen et al. (2014), no turbulence closure was used to describe the flow taking place in the vicinity of the porous media. However, in the paper, it is reasoned that the turbulence effects would be taken care via Darcy-Forchheimer equation. Further, it is mentioned that the experiments considered in the study of Jensen's study involved little or no wave breaking effects and hence the turbulence was not modeled separately in the study. Further, it is argued that the turbulence closure is essential only if the information pertaining to the actual level of turbulence inside the porous media is of interest. Jensen's study states the resistance coefficients obtained by the process of calibration involving experimental results will have inherent turbulence effects. Hence, by using the resistance coefficients in the numerical model, the dissipation effects arising due to turbulence will be accounted for. It is therefore mentioned here to stay cautious in the usage of resistance coefficients from literature. The resistance coefficients obtained using the numerical model without using turbulence closure would produce higher values in comparison with a numerical model incorporating turbulence closure (Jensen et al., 2014; Losada et al., 2016). In the present study, the turbulence inside the porous media is not considered. However, this would be accounted for through the resistance coefficients (Jensen et al., 2014) obtained during the process of calibration. For the regions outside the porous media, turbulence modeling has been carried out using two-equation $k-\omega$ model (where, k - turbulent kinetic energy and ω - specific turbulence dissipation rate.

2.5 Numerical Wave Tank

A schematic sketch of the numerical domain is presented in Figure 1. Wave generation is carried out using the relaxation method (Engsig-Karup, 2008). A detailed description of the governing equations and numerical implementation using REEF3D can be found in Bihs et al. (2016). The numerical beach is modeled using active wave absorption based on the shallow water theory (Schäffer and Klopman 2000) and seen to provide good wave absorption properties even if the generated waves do not conform to the shallow water theory (Miquel et al. 2018, Sasikumar et al. 2018). Since the VRANS approach involves the calibration of the resistance coefficients, care has been taken to make sure that the numerical model remains identical with the experimental setup. Three wave gauges (η_1, η_2, η_3) are positioned at a distance of 18, 28.65 and 39.25 m from the wave inlet to measure the wave elevations at the respective points as shown in Figure 1. A grid resolution study is carried out in order to ascertain the accuracy of the model. The details of the grid resolution study is presented in Figure 2 where the experimental measurements from published work (Srineash and Murali 2019) are compared with the simulations with varying grid sizes. Further details pertaining to the experiments are presented in the forthcoming section. For the grid resolution study, the number of grid cells considered were 2×10^5, 3×10^5, 4×10^5 and 5×10^5 cells. Stokes second-order waves with wave period $T = 1.4$ s corresponding to a wavelength $L = 2.14$ m and wave amplitude $a = 0.024$ m is generated in the numerical wave tank. The relative water depth d/L considered for the grid resolution study is 0.14. On perceiving the results

presented in Figure 2 it is noticed that the results start converging from the case with 3×10^5 onwards. However, the case with 4×10^5 and 5×10^5 cells is seen to reproduce results close to experiments. Considering the computational time, the grid with 4×10^5 cells is chosen for the study. Therefore a non-uniform rectilinear grid consisting of 4000 cells along the direction of wave propagation and 100 cells in the vertical direction is used. The computational time for a given simulation in the discussed numerical setup is 1 hour using a computational facility with 128 processors. Grid stretching function is used in the study to get finer girds in the vicinity of the porous structure. The finest grid near the porous structure is with dx=0.005 and dy=0.008 whereas the coarsest grid is with dx=0.018 and dy=0.014 near the boundary.

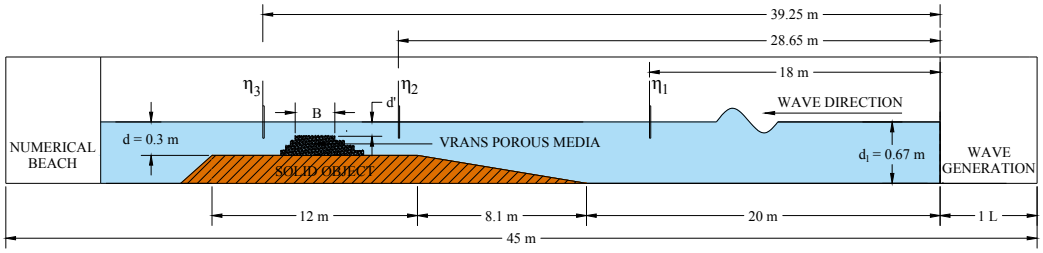

Figure 1: Computational domain for wave transmission studies with the location of wave gauges (η). The porous media portrayed is modeled based on VRANS approach. For further details pertaining to the range of wave parameters considered, refer Table 1 and the Methods section.

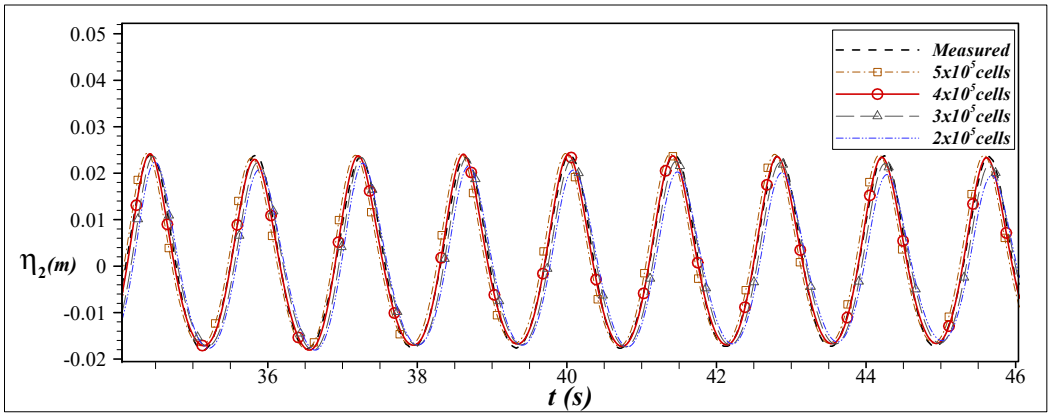

Figure 2: Grid refinement study adopted in the present study. The experimental results are compared with the simulations involving varying grid sizes consisting of 2×10^5, 3×10^5, 4×10^5 and 5×10^5 cells. Further details regarding the grid description can be found in the Numerical Wave Tank section.

2.6 Calibration of the resistance coefficients in the VRANS equations

Determination of empirical coefficients, α (linear resistance coefficient) and β (non-linear resistance coefficients) are essential in the study involving wave interaction with porous structures. This process of calibration of the numerical model to determine α and β values are

crucial since these coefficients are seen to govern the flow inside the porous media (Garcia et al. 2004). These coefficients have their direct implication on Darcy–Forchheimer equations as discussed previously. The calibration of the numerical model is often performed by comparing it with the physical model experiments (Garcia et al. 2004, Liu et al. 1999, Jensen et al. 2014, Losada et al. 2016). A systematic procedure is adopted for calibration of α and β for which a calibration range with α = [200, 400, 500, 600, 800, 1000] and β = [1.1, 2.2, 3.3, 4.4] is chosen. From the analysis based on simulations involving various α and β values, the best match with the experiments is noticed for the simulation with α = 500 and β= 3.3. It is emphasized here that there is a wide range of α and β values described in the literature. The work carried out by Losada et al. (2014), Lin and Karunarathna (2007) document the presence of a wide range of α and β values. This clearly indicates the need for attention in modeling wave interaction with porous structures. Further, it has been emphasized (Liu et al. 1999) that the accuracy of modeling the wave interaction with porous structures has a direct implication on the empirical resistance coefficients (α and β) that are adopted to represent the flow through the porous media. The numerical model calibration is carried out with experimental measurements as a reference for which waves with $T = 1.4$ s and $a = 0.024$ m is chosen corresponding to a $d/L = 0.14$.

2.7 Influence of resistance coefficients (α and β) on the wave elevation

The influence of the resistance coefficients (α and β) on the transmitted wave profile is carried out in this section. The purpose of such a study is to demonstrate the sensitivity of the results due to variations in resistance coefficients. In order to understand the relative influence of α and β on the wave elevation, the results are presented for a constant β with varying α (Figure 3) and, constant α with varying β (Figure 4). Figure 3 and Figure 4 present wave elevation results at η_3 which pertains to a relative depth, d/L =0.14. The results are illustrated in the figures for α=200,500 and 1000 and β=1.1, 2.2 and 3.3. In Figure 3 and Figure 4, the time-series history is presented in (a), (b) and (c) and a magnified version pertaining to a wave cycle is depicted in (d), (e) and (f). This is done so that the features of the transformed wave containing dispersive tail waves can be appreciated with the variations in resistance coefficients. An overall analysis of the figures brought out indicates that the influence of the resistance coefficients on the transmitted wave profile is less as far as the magnitude of wave heights are concerned. However, there is a marginal influence on the shape of the transmitted wave train, which is of less significance for quantifying the hydrodynamic performance of coastal structures. Therefore, it can be presumed that the results from the present study can be used for coastal structures with typical porosities and grain sizes. Given that in the case of coastal structures, the typical porosities and grain size diameters chosen in the design are quite similar and the required values of alpha and beta can be deduced from past experimental studies. It is also seen from recent works of Sasikumar et al. (2019) and Kamath et al. (2019) that values from existing literature such as Troch, P. (2000) can be safely used to perform such simulations involving wave interaction with porous structures. Therefore, the values chosen for alpha and beta in the current study can be considered useful for further studies involving typical porous coastal structures usually encountered.

On interpreting the features from Figures 3(d), (e) and (f), it can be noticed that the effects due to variations in β for constant α is non-appreciable. The effects due to variations in β is almost negligible for α =500 and 1000 as perceived from Figures 3(e) and (f). Further,

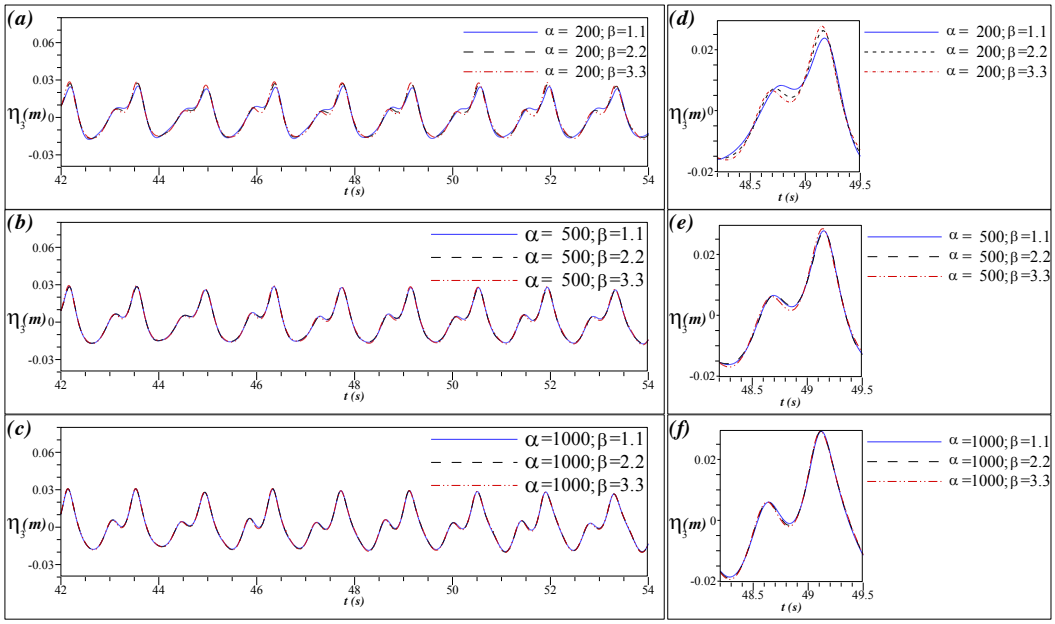

Figure 3: Variations in nonlinear resistance coefficients (β) for constant linear resistance coefficients (α) and its influence on wave elevation at η_3. The typical time-series history for varying β and constant α is presented in (a), (b) and (c) and a magnified version pertaining to a given wave cycle is indicated in (d), (e) and (f).

a similar interpretation of results for variations in α for constant β as noticed from Figures 4(d) (e) and (f) reveals that the features in the wave profile are sensitive to α. Therefore, this gives a perception that the linear resistance coefficient (α) has a higher bearing in affecting the features (shape) of the transmitted wave profile in comparison with the nonlinear resistance coefficient (β). These aspects are brought out in Figure 3 and Figure 4.

2.8 Experimental Measurements

For the purpose of calibrating the numerical model and to perform a comparative study, the results from experiments are used. The experimental measurements used for the present study are carried out in the 72 m long shallow water wave flume of the Department of Ocean Engineering, Indian Institute of Technology Madras, India. More details of the test facility are described in Srineash and Murali (2018). The wave flume discussed in the present study has been used for conducting various coastal engineering experiments and has been used demonstrated to have good wave absorption capability (Krishnakumar et al., 2009, Murali, 1996, Srineash and Murali, 2018). The details of the experimental setup are provided in Figure 5. In experiments, the porous structure is built with gabion box models and hence the structure has a stepped slope. The porosity of the porous media is 0.37 with the median stone size (d_{50}) being 0.01 m. The details pertaining to the experimental setup and gabion box models may be found in Srineash and Murali (2015) and Srineash and Murali (2019). Resistance type wave probes were used for the measurement of instantaneous wave elevations and the location of wave probes are presented in Figure 5. A detailed experimental study

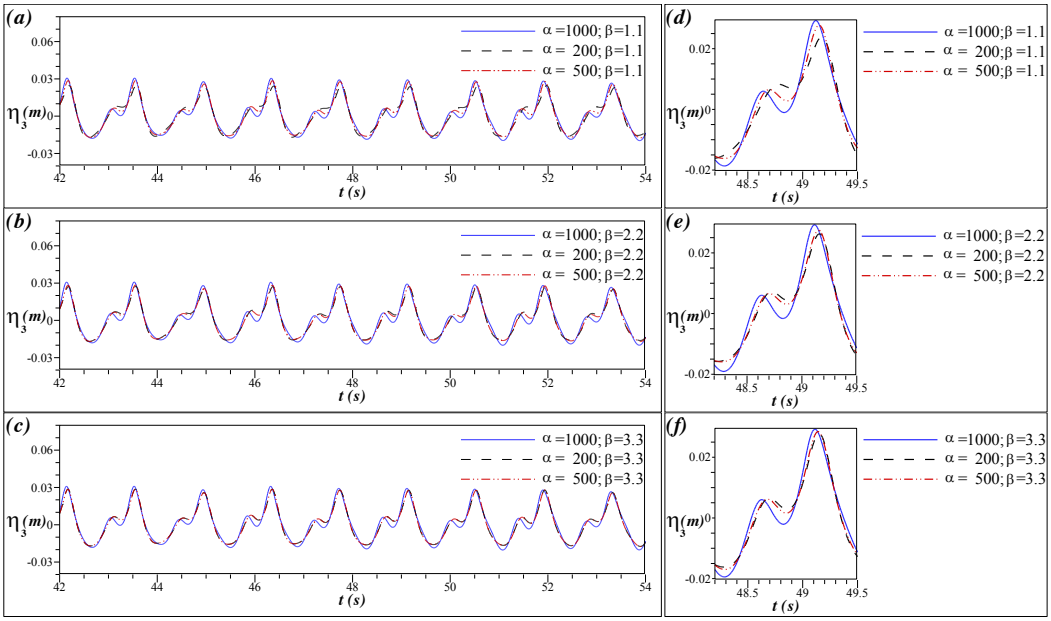

Figure 4: Variations in linear resistance coefficients (α) for constant nonlinear resistance coefficients (β) and its influence on wave elevation at η_3. The typical time-series history for varying α and constant β is presented in (a), (b) and (c) and a magnified version pertaining to a given wave cycle is indicated in (d), (e) and (f).

involving the functional performance of submerged porous reef breakwaters are presented in Srineash and Murali (2019); in the present research, typical experimental results are used from the experimental study for calibration of the numerical model and for validation. Pressure probes were used for the measurement of pressures at various locations around the porous structure and detailed location of pressure probes are brought out in Figures 6. A sampling frequency of 40 Hz was used for data acquisition during the experimental measurements.

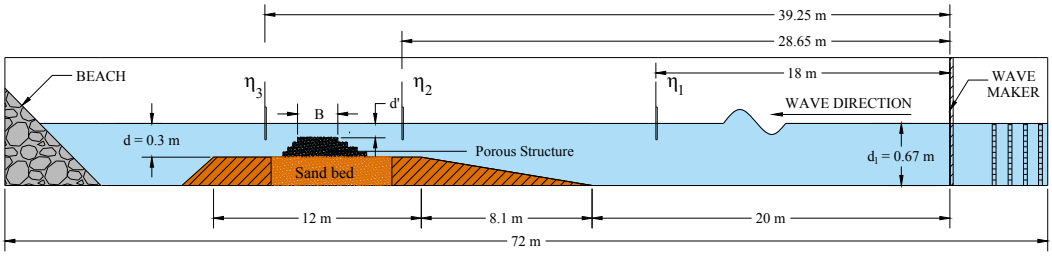

Figure 5: Experimental setup considered in the present study with the location of wave gauges. The experiments were performed in 72 m long shallow water wave flume. More details pertaining to the experimental facility and setup can be found in Srineash and Murali (2019).

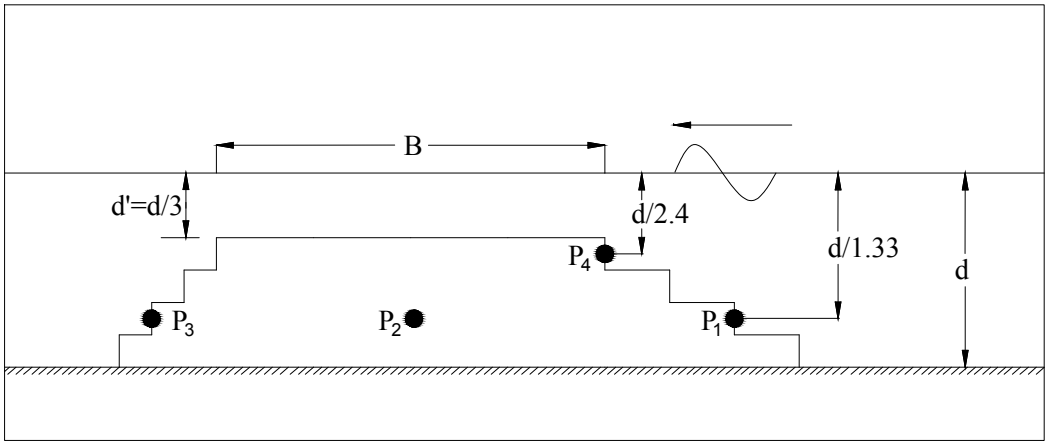

Figure 6: Schematic sketch of the geometric configuration and arrangement of pressure probes. The study consists of four pressure probes P1, P2, P3 and P4 to measure the hydrodynamic pressures over the porous media. The pressure probes P1, P2 and P3 are in line and placed at a distance of $d/1.33$ from the free surface. The probes P1 and P3 measure the hydrodynamic pressure on the seaside and the leeside direction of the porous structure. The probe P2 measures the pressure inside the porous media at the mid-section of the structure.

3 Results

The numerical results from the model adopting VRANS equations to represent the porous media is compared with the experimental measurements. The comparison has been carried out for the free surface elevation and the pressure-time history for varying crest width ratios. The velocity contours depicting the evolution of wave breaking is presented. Further, the investigation studies the wave transmission for a range of wave parameters and geometric configuration of the porous media. The numerical results for the free surface elevation are also analyzed in the frequency domain in order to understand the effects of energy redistribution to the higher harmonics. Finally, the formation of the wave envelope as the wave transforms past the porous media is visualized.

3.1 Comparison of numerical results with measurements

To demonstrate the effectiveness of VRANS modeling in simulating the process of wave interaction with submerged porous media, a comparison of numerical simulations with the experiments is carried out. For this, suitable resistance coefficients are identified by calibration which are $\alpha = 500$ and $\beta = 3.3$ using experimental results for the case with crest width $B = 2d$. The numerical simulations are carried out for three crest widths $B = d$, $B = 2d$, $B = 3d$. The wave and pressure measurements are performed in the experiments. For the present comparative study, the placement of wave gauges and pressure probes in the numerical model has been carried out similar to the experiments. The positioning of the wave gauges in the NWT has been already discussed. Four pressure probes ($P1$, P_2, P_3, P_4) are positioned on the porous media and the resulting pressure head (P/γ) is compared. Where, γ is the specific weight of water. Figure 6 portrays a typical configuration of porous media with crest

widths $B = d$ along with the location of pressure probes in the porous media. The water depth (d =0.3 m) and depth of submergence ($d' = d/3$) of the porous media (structure) is maintained constant throughout the study. The pressure probes P_1, P_2 and P_3 are in line and placed at a distance of $d/1.33$ from the free surface. The probes P_1 and P_3 measure the hydrodynamic pressure on the seaside and the leeside direction of the porous structure. Whereas, the probe P_2 captures the pressure inside the porous media at the mid-section of the structure. The probe P_4 is located at a distance of $d/2.4$ below the free surface as portrayed in Figure 6. The probe P_4 captures the seaside pressure near the crest of the porous media. The effective slope of the porous structure is 1:2 in the seaward direction and 1:1 in the shoreward direction. The only difference between the experiments and the simulations is that a porous sand bed is used during the experiments. This is not considered in the numerical simulations owing to the lower hydraulic conductivity of sand bed which is 0.00078 m/s in comparison with the porous media which takes a value of 0.38976 m/s.

3.2 Comparison of free surface elevations

The free surface elevation records are measured at a distance of 18, 28.65 and 39.25 m from the wave inlet as depicted in Figure 1. A comparative study involving free surface elevations (η_1, η_2, η_3) in the numerical simulations and the experiments is carried out and presented in Figure 7. In the Figure 7(a), the records of the free surface elevation (η_1) at a distance of 18 m from the wave inlet is presented in the time domain. The free surface elevations show a good agreement and this demonstrates that the simulated wave field on the seaside of the structure is identical to that in the laboratory measurements.

Figure 7(b) and (c) correspond to the configuration with crest width $B = d$. The time series of the wave elevation (η_2) in front of the porous structure is depicted in Figure 7(b). From Figure 7(b), the numerical simulation and the experimental measurements seem to agree well. The wave gauge η_2 includes the effect of shoaling due to the presence of the submerged ramp and the influence of reflection from the porous structure. The agreement of the numerical simulation with the experiments signifies the effectiveness of VRANS approach in reproducing the physical process taking place in front of the porous media as inferred from Figure 7(b).

The transmitted wave profile recorded on the wave gauge (η_3) pertaining to a configuration with $B = d$ is shown in Figure 7(c). In Figure 7(c), the presence of multiple wave crests due to wave decomposition which occurs as the wave interacts and transforms past the porous structure is observed. This phenomenon is called amplitude dispersion. This complex wave profile with multiple crests, also referred to as dispersive tail waves, is due to the presence of higher harmonics in the transmitted wave profile which has been reported earlier by the past researchers (Beji and Battjes 1993, Dattatri et al. 1978, Garcia et al. 2004, Hall and Seabook 1998, Johnson et al. 1951). On analyzing the time series of η_3 for configuration $B = d$ in Figure 9(c), one may notice that the numerical model is capable of representing the transmitted wave profile including the dispersive tail effects appropriately as seen in experiments, using the VRANS approach.

Figures 7(d) and (f) belong to the configurations with crest width $B = 2d$ and $3d$ respectively. As discussed for the wave profile in Figure 7(b) pertaining to $B = d$, the configuration with B=2d and 3d is noticed to capture the effects such as wave shoaling and reflection in front of the porous structure as in case of experiments. On analyzing the Figures 7(e) and

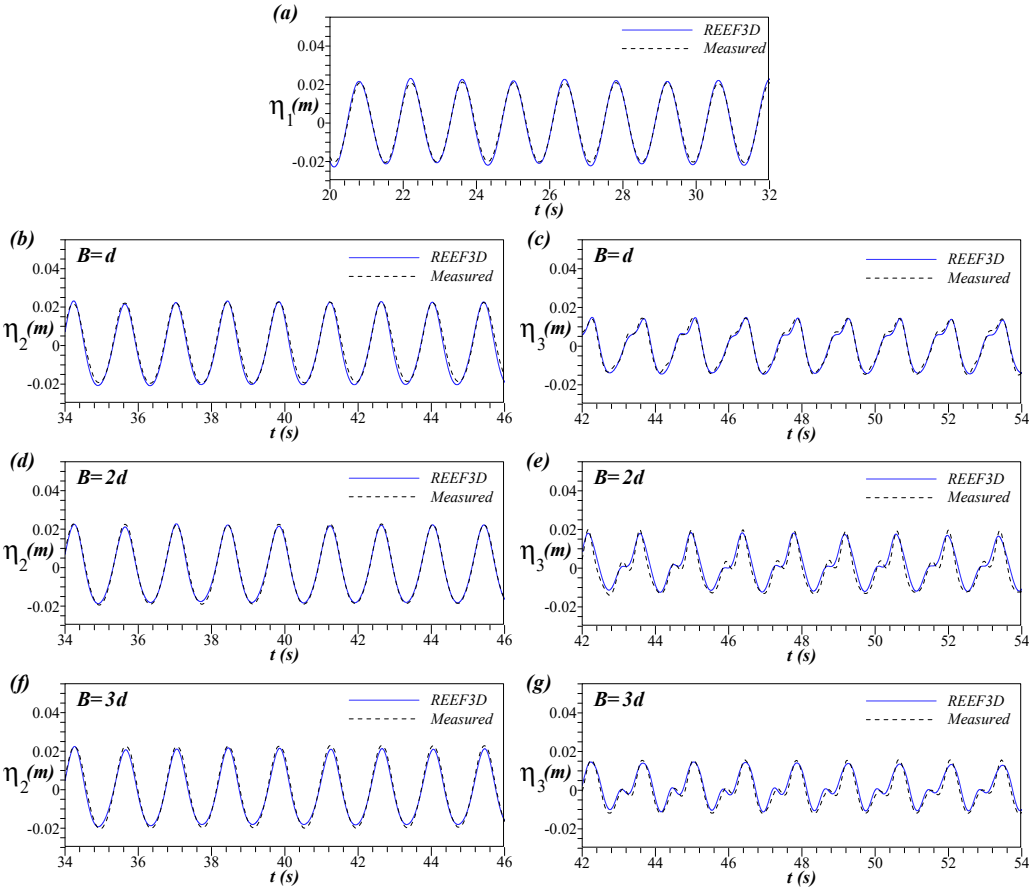

Figure 7: Comparison of wave elevation obtained from experimental measurements with numerical simulations with varying crest widths. The comparison has been portrayed for wave elevation measurements at η_1,η_2 and η_3 located at a distance of 18, 28.65 and 39.25 m respectively from the wave inlet. The wave elevation results at η_1 is brought out in (a). The wave elevation results at η_2 is depicted in (b), (d) and (f) for porous structure with crest widths of $B = d$, $B = 2d$ and $B = 3d$ respectively. Similarly, the wave elevation results at η_3 is illustrated in (c), (e) and (g) for porous structure with crest widths of $B = d$, $B = 2d$ and $B = 3d$ respectively.

(g) containing the transmitted wave profiles (η_3) it is noticed that the simulations are able to reproduce the free surface elevations similar to experiments and the dispersive tail waves are well represented in the numerical simulations. The decrease in the free surface elevation of the transmitted wave profile with an increase in crest width (B) is also noticed on comparing results from the Figures 7(c), (e) and (g). The wave decomposition due to the complex interaction of wave train with the submerged porous structure becomes prominent with an increase in crest width (B) as the dispersive tail waves are noticed to become pronounced with the rise in crest width. These aspects reinforce the applicability of VRANS approach in modeling the wave interaction in the vicinity of the porous structures.

3.3 Pressures measurements in and around the porous structure

The measurement of pressures on the seaward side and leeward side of the porous structure has been carried out along with the pressure measurement inside the porous media as illustrated in Figure 6. The pressure probe P_4 measures the wave pressure close to the seaward crest of the porous structure (at a distance $d/2.4$ from the still water level) and hence this pressure probe is seen to record a maximum pressure value as noticed from Figure 8(a). The pressure head (P/γ) recorded from P_4 is seen to record the crest pressure head (maximum pressure head occurring during the wave crest) of about 0.022 m for the configuration with $B = d$. A similar magnitude of pressure head noticed for the pressure probe P_4 for configuration $B = d$ and $B = 2d$ which takes the value of 0.021 m as depicted in Figure 9(a) and Figure 10(a) and these aspects are well represented by the numerical model.

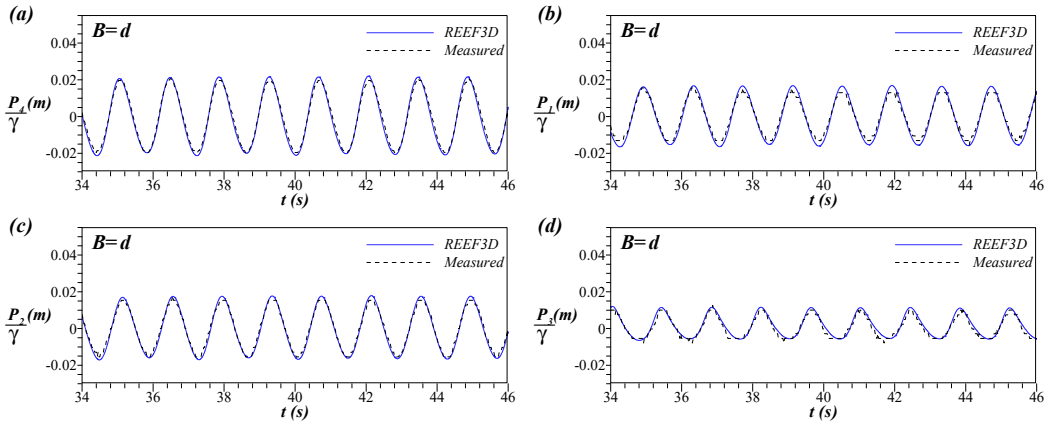

Figure 8: Comparison of pressure head (P/γ) from experimental measurements with numerical simulations for crest width $B = d$, for pressure probe locations at P4, P1, P2 and P3 in (a), (b), (c) and (d) respectively.

The pressure probes P_1, P_2 and P_3 are located in-line at a distance $d/1.33$ from the still water level. The pressure probe $B = d$ is located at the seaward face of the porous structure with a distance of $d/1.33$ vertically below the still water level. The crest pressure head pertaining to $B = d$, $B = 2d$ and $B = 3d$ [From Figures 8(b), 9(b) and 10(b)] for the probe P_1 is seen to take values close to $P_1/\gamma = 0.018$ m. However, for the pressure probe present inside the porous structure, P_2 there seems to be a decrease in pressure head with an increase in crest width and this is evident from Figures 8(c), 9(c) and 10(c). It is also noticed that the extent of pressure damping inside the porous media between the configurations with $B = d$ and $B = 2d$ is significant when compared to the pressure damping (P_2/γ) for $B = 2d$ and $B = 3d$. There is a 28% reduction in the crest pressure head (for the probe P_2) P_2/γ, on change of crest width from $B = d$ to $B = 2d$ and this effect is captured by the numerical model. On analyzing the wave crest pressure head on the lee side of the porous structure (P_3), there seems to be no notable difference in the pressure as a similar value of pressure head is observed for configurations with varying crest widths ($B = d$, $B = 2d$, and $B = 3d$). However, from the wave gauge readings pertaining to the transmitted wave profiles (η_3), the wave attenuation is seen to increase with an increase in the crest width, hence analyzing the wave kinematics on the porous media may help in the understanding of the processes

taking place leading to such effects. The minimum crest pressure head observed among the probes P_1, P_2, P_3 and P_4 is noticed to correspond with the probe on the leeside of the porous media (P_3) which takes the value of $P3/\gamma$ around 0.012 and this has been observed during experiments and simulations. Overall, from the analysis of the pressures on the porous media, the numerical model is able to reproduce the hydrodynamic pressures on the seaside, the lee side and inside the porous media as observed during experiments.

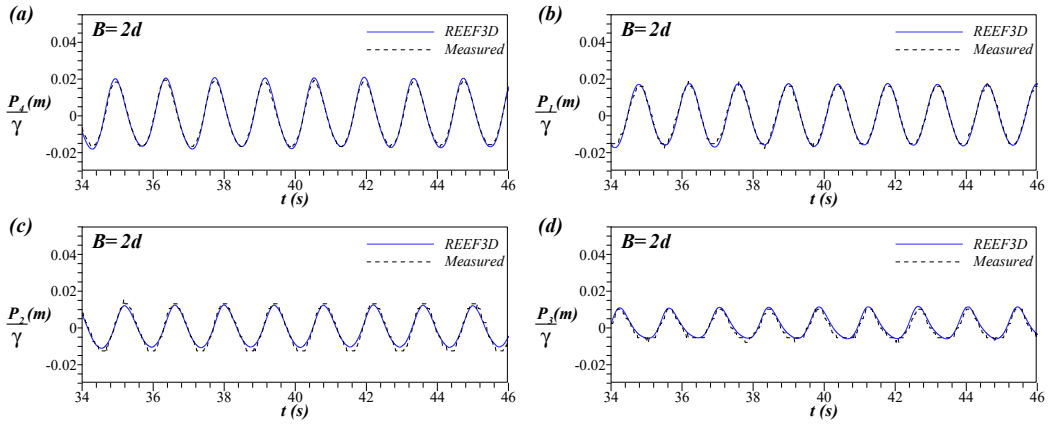

Figure 9: Comparison of pressure head (P/γ) from experimental measurements with numerical simulations for crest width $B = 2d$, for pressure probe locations at P4, P1, P2 and P3 in (a), (b), (c) and (d) respectively.

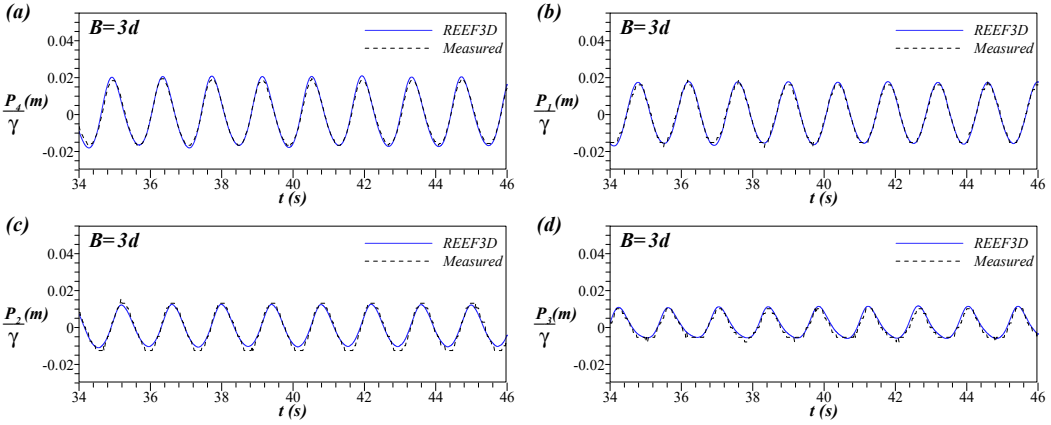

Figure 10: Comparison of pressure head (P/γ) from experimental measurements with numerical simulations for crest width $B = 3d$, for pressure probe locations at P4, P1, P2 and P3 in (a), (b), (c) and (d) respectively.

3.4 Numerical investigation of wave transmission

In order to investigate the effect of crest width in wave transformation, further investigations are conducted to study the influence of the wave and geometric parameters ($B = 2$, $2d$

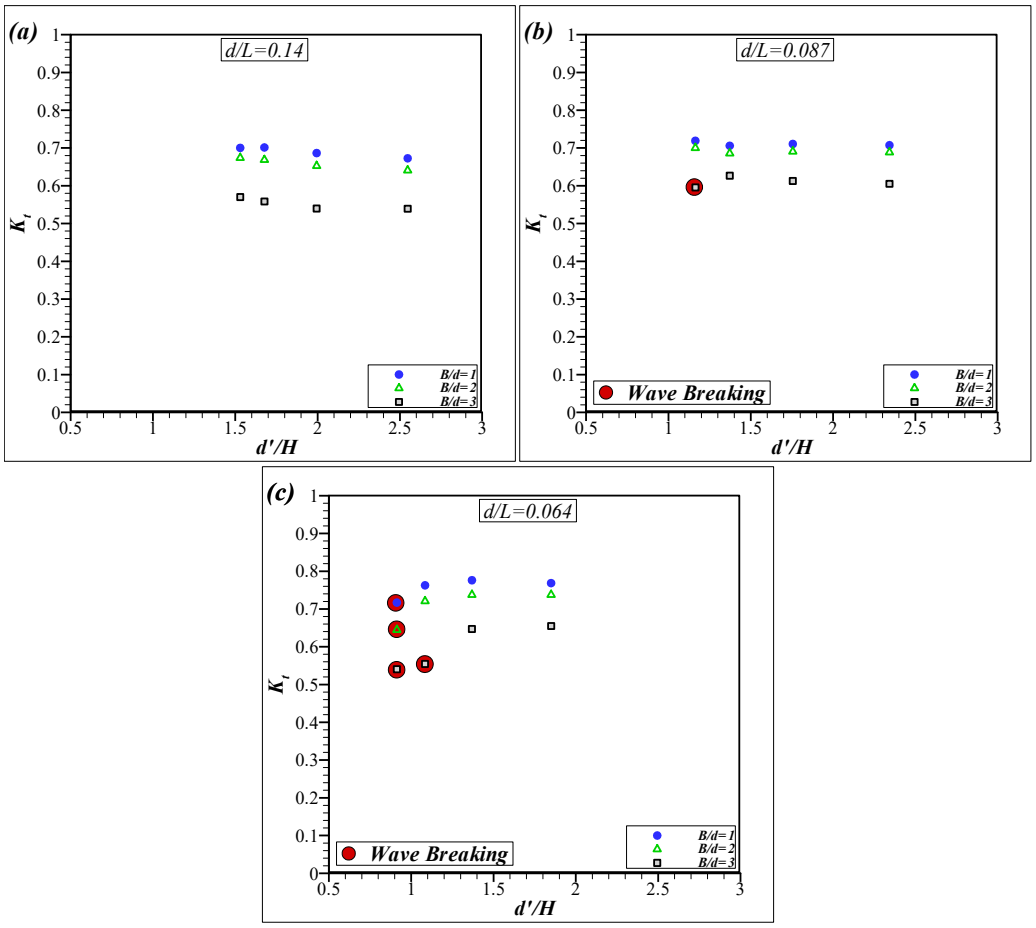

Figure 11: Variation of transmission coefficient (K_t) with d'/H for B/d=1-3. The tests leading to wave breaking due to the presence of the reef are represented with a red circle. The wave attenuation characteristics for d/L= 0.14, 0.087 and 0.064 has been depicted in (a), (b) and (c) respectively.

and $3d$) on transmission coefficient (K_t). The range of dimensional and non-dimensional variables considered in the present study is depicted in Table 1 and 2 respectively. It is seen from past studies (Ahrens 1987, Briganti et al. 2003, d'Angremond et al. 1996, Tanaka 1976, van der Meer and Daemen 1994, van der Meer et al. 2005) that the relative depth of submergence (d'/H) is the major variable governing wave transmission over submerged low crested structures hence K_t is studied with respect to d'/H as portrayed in Figures 11(a), 11(b) and 11(c). The variation of K_t with d'/H for d/L of 0.14 is portrayed in Figure 11(a). From the figure, it is noticed that the wave attenuation increases with an increase in B/d. This is in accordance with the observation made by Tanaka (1976) and Sasikumar et al. (2018). It is expected that the wave transmission reduces with a reduction in d'/H. However, this is true when there is a strong interaction of the submerged structure with the wave field. In the present case with $d/L = 0.14$, the d'/H is seen to take higher values ($d'/H > 1.5$) where a strong interaction waves with the submerged structure may not be anticipated and

hence a marginal increase of K_t is observed with a reduction in d'/H. This behaviour was also observed during the experimental investigations as reported in Srineash and Murali (2019). These aspects increase the confidence in adopting a numerical model incorporating RANS equations for such exercise.

A similar examination is carried out for $d/L = 0.09$ (Figure 11(b)) where the range of d'/H varies from 1.16 – 2.34. It is interpreted from Figure 11(b) that K_t is almost constant and the interaction of the wave with the structure is more pronounced for lower d'/H and higher B/d values. From Figure 11(b) the data corresponding to the highest B/d (=3) and lowest d'/H (=1.16) is noticed to undergo wave breaking which is distinguished by a clear difference in the wave transmission pattern. One may observe the highest wave attenuation during wave breaking due to the presence of the structure [the cases involving wave breaking is highlighted in Figure 11(a) and 11(b)]. For the case with the lowest d/L considered in the study (d/L =0.064) as depicted in Figure 11(c), the d'/H ranges from 0.91 – 1.85. The effects of wave interaction with the structure seem to be pronounced for lower d'/H and there is wave breaking noticed when d'/H approaches 0.91. The wave breaking is also observed at $d'/H = 1.08$ for the highest B/d this is due to the prominent effect of structure on the wave transmission for longer waves. From Figure 11(c), the K_t is noticed to decrease with a decrease in relative depth of submergence (d'/H) for d'/H <1.5. Overall from the numerical study, it is observed that wave attenuation increases with a decrease in relative depth of submergence (d'/H) and an increase in crest width ratio (B/d). Further, the investigation reveals that the wave breaking induced due to the presence of the porous structure facilitates in achieving significant wave attenuation.

3.5 Velocity Contours

The velocity contours during the wave interaction with the porous reef breakwater are brought out here. This is carried out to establish the application of the numerical model to investigate the water particle kinematics in the vicinity of the porous structure. The horizontal water particle velocity, u_x around the porous structure is depicted. The information on the magnitude of velocity in the direction of wave propagation along with its distribution is a vital engineering aspect to look into.

Further, the velocity distribution can be associated to the wave-induced forces acting on the structure (Lara et al. 2006). Morison's method of wave force calculation needs velocity information which can be ascertained from velocity magnitudes. Additionally, assessment of the stability of the structure can be related to the water particle kinematics near the vicinity of the structure. Furthermore, the information pertaining to velocity may be used to identify the potential zones for marine growth. In recent times, submerged porous structures are built also to enhance marine species and are often referred to as 'Artificial Reefs' (Srineash and Murali 2015).

The velocity contours in the numerical wave tank are presented in this section for the configuration with crest width $B = 3d$ in Figure 12. The contours display the values of the horizontal velocity. The velocities at time instants $t/T = 30.53$, 30.78, 31, 31.14 are presented in Figures 12(a), 12(b), 12(c) and 12(d) respectively [where, t is the simulation time]. This is done to demonstrate the process of wave breaking taking place as the wave travels past the submerged porous structure. The figures display wave interacting in front of the porous structure Figure 12(a) and wave propagating over the crest of the structure as displayed in

Figure 12(b). The incident waves traveling over the crest of the porous structure undergo a strong interaction leading to a reduction in wave celerity. The horizontal water particle velocity in the wave crest exceeds the celerity of the wave and the wave curls over leading to wave breaking. This wave breaking induced due to the presence of the porous structure is witnessed in Figure 12(c) and in the wave transmission past the porous structure in Figure 12(d). It is seen that the magnitude of horizontal velocity during the wave breaking takes the value as high as 2.2 m/s. This case corresponds to a d/L of 0.064. One can also observe the wave attenuation on the lee side of the porous structure. Thus, the model serves as a useful tool to infer the wave characteristics and the complex hydrodynamics in the vicinity of the porous media.

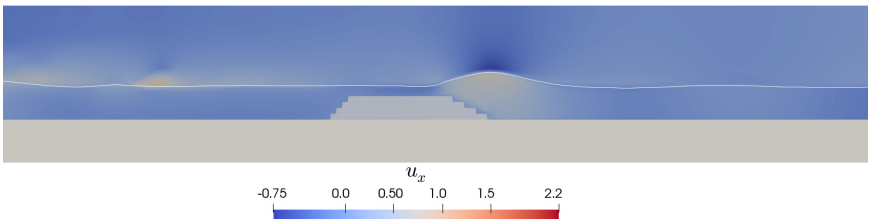

(a) t/T=30.53

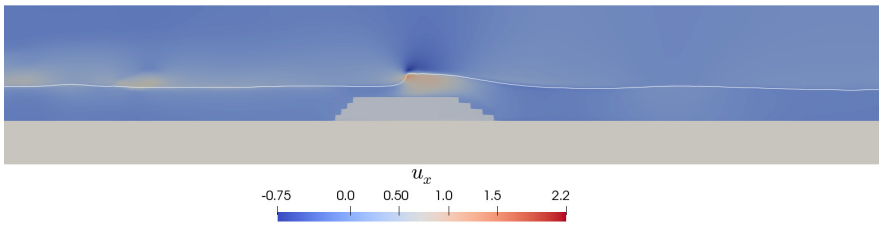

(b) t/T=30.78

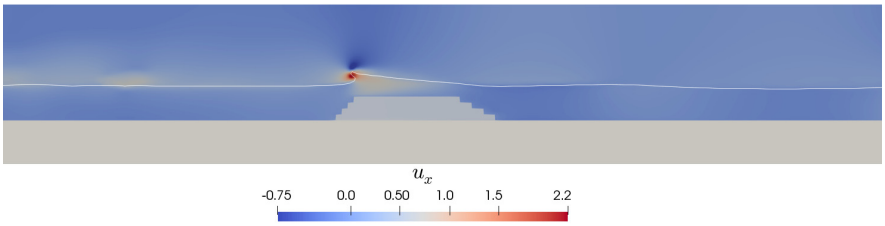

(c) t/T=31.00

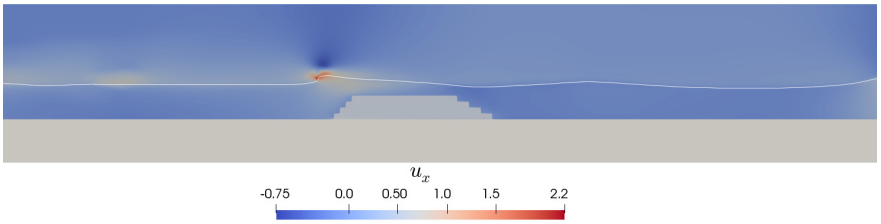

(d) t/T=31.14

Figure 12: Wave transmission past the porous media for $B = 3d$ and the evolution of wave breaking with horizontal velocity contours

3.6 Wave decomposition and frequency analysis

For understanding the wave transformation process over the porous media, a frequency domain analysis is carried out with the incident and the transmitted wave profiles. This is done by decomposing the free surface elevation using Fast Fourier Transform (FFT) algorithm. This frequency domain analysis has been carried out for various wave parameters and the crest widths of the porous structure as depicted in Figure 13. The plots in Figure 13 represents an increase in crest widths horizontally and a decrease in relative water depth (d/L) vertically. This analysis has been carried out for $B = d$, $2d$, $3d$ and $d/L = 0.14$, 0.087, 0.064. In Figure 13, the x-axis displays the normalized frequency [which is the ratio of discrete frequency to the fundamental frequency (f/f_0)] while the y-axis denotes the normalized power spectral density (S/S_{max}). The power spectra are normalized with the power spectral density corresponding to the fundamental frequency (f_0) of the incident wave which is Smax. From Figure 13(a) which corresponds to $d/L = 0.14$ and crest width $B = d$, it is noted that in the fundamental frequency (i.e., $f/f_0 = 1$), the transmitted normalized power spectral density (past the porous media) is about 0.43 which denotes a 57% reduction in energy in the fundamental frequency. On making a similar interpretation for Figures 13(b) and 13(c) which relates to $B = 2d$ and $3d$, respectively the transmitted S/S_{max} value reach 0.36 and 0.21. This denotes the effectiveness of the crest width of the porous structure aiding wave attenuation as one may observe an increase in wave attenuation with an increase in crest width. For the case with d/L =0.14, the lowest transmitted S/S_{max} value is 0.21 which denotes a reduction in energy of 79% in the fundamental frequency. However, it is to be mentioned that there is a redistribution of energy to higher harmonics for the transmitted spectrum as observed in Figures 13(c) [$B = 3d$]. The maximum energy redistribution is observed until the second harmonic for the transmitted wave profile of $d/L = 0.14$.

On investigating Figures 13(a), 13(d) and 13(g) that belong to same crest width ($B = d$) but varying d/L (d/L =0.14, 0.087 and 0.064) one can note that with decrease in d/L the redistribution of energy to higher harmonics becomes evident and this is noticed for both incident and transmitted wave profiles. This is due to the effect of amplitude dispersion (Beji and Battjes 1991) which becomes pronounced at lower d/L. This amplitude dispersion is reported for long waves, $f = 0.4$ Hz. It is worth mentioning here that the case with $d/L = 0.064$ corresponds to a wave frequency of $f = 0.36$ and hence this redistribution of energy to higher harmonics is expected for the incident and transmitted waves. In Figure 13(g) the incident and the transmitted spectrum is observed to be prominent till the second harmonic. However, the energy redistribution in the case of the transmitted spectrum is noticed till the fifth harmonic. There is also a trend of a marginal increase in the value of transmitted S/S_{max} observed with a decrease in d/L. On analyzing Figures 13(d), 13(e) and 13(f) having d/L =0.087 and $B = d$, $2d$, $3d$ the wave attenuation is noticed to increase with the increase in crest width. The redistribution of energy to the higher frequencies is observed to be prominent with an increase in crest width. The maximum energy redistribution is noticed to be seen until the fourth harmonic for the transmitted wave profile of $d/L = 0.087$. As noted earlier, the highest crest width ($B = 3d$) accounts for the maximum wave attenuation with S/S_{max} reaching 0.28 denoting about 72% reduction in the energy level in the fundamental frequency as observed from Figure 13(f). Further the Figures 13(b), 13(e) and 13(h) represents a constant crest width ($B = 2d$) but with varying $d/L = 0.14$, 0.087and 0.064 respectively. A similar observation as noted for cases with $B = d$ is observed for $B = 2d$ implying an

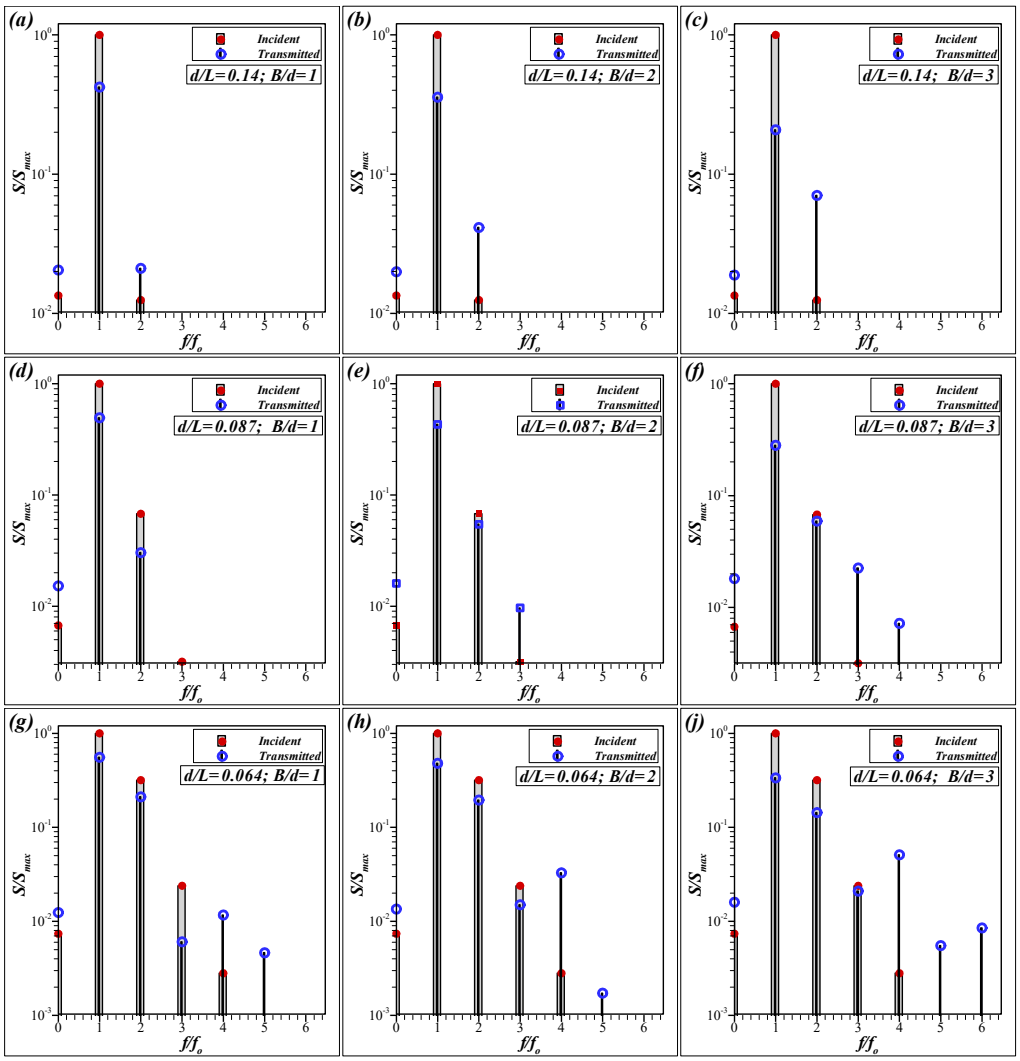

Figure 13: Energy specra of Incident and transmitted waves for varying wave parameters and crest widths. The x-axis displays the normalized frequency [which is the ratio of discrete frequency to the fundamental frequency (f/f_0)]. The y-axis denotes the normalized power spectral density (S/S_{max}). The power spectra are normalized with the power spectral density corresponding to the fundamental frequency (f_0) of the incident wave which is S_{max}.

increase in energy redistribution to higher harmonics with a reduction in d/L and a marginal reduction in wave attenuation with a decrease in d/L. The same is valid for the case with $B = 3d$ across the d/L considered. Also for a constant $d/L = 0.064$ (Figures 13(g), 13(h) and 13(j)), the presence of higher harmonics becomes more evident with an increase in crest width as the energy redistribution of the transmitted wave train is noticed till sixth harmonic. These aspects reveal that an increase in crest width (B) and a reduction in d/L influences and amplifies the energy redistribution of the transmitted wave spectrum. From the frequency domain study, it is noticed that the maximum wave attenuation takes place for the case with

the maximum crest width and higher d/L. The minimum wave attenuation is recorded for the case with the minimum crest width and lower d/L.

3.7 Numerical study on pressure reduction due to reef breakwater placed in tandem to a seawall

The frequent occurrence of storms coupled with sea-level rise issues has made the shorelines and the coastal infrastructure vulnerable. It is essential to come up with engineering solutions that are capable of tackling the above-mentioned issues. The use of reef breakwaters in tandem to the existing structure will reduce the wave load on the existing structure. The pressure reduction realized due to the presence of the reef breakwater placed in tandem (on the seaside) to a vertical seawall is taken up in the present study. Such studies are applied to combat climate change mitigation issues and to reduce wave loads on existing structures that have undergone excessive loading (Sasikumar et al., 2018). This can be witnessed from the studies made by Koraim et al (2014), Madrigal and Homme (1991) and Reddy and Neelamani (2005). Such studies are important in situations where the prevailing wave conditions on the coast exceed the design conditions considered during the design of the structure. In such cases, where the wave conditions have become severe, due to factors such a climate change, submerged structures can be built in tandem which will facilitate wave attenuation.

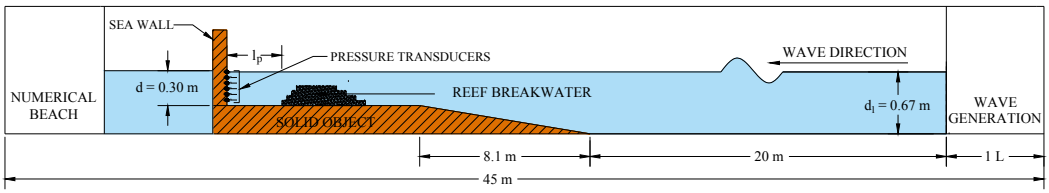

Figure 14: Computational domain demonstrating the use of tandem reef breakwaters to reduce wave-induced pressures on the leeward seawall. The location of the pressure gauges at various levels on the seawall is illustrated. The pressure gauges were located at z/d= 0, (-)0.17, (-)0.33, (-)0.50, (-)0.67 and (-)0.83.Where, z is the point of interest and defined negative below still water level. The length of the pool (l_p) is the distance between the seawall and the reef breakwater.

A schematic sketch of the NWT used during the investigation is depicted in Figure 14. The wave tank consists of a vertical seawall defended by a porous reef breakwater. There are pressure probes used in the study to capture the pressures on the seawall. The numerical simulations were performed in two cases, one considering only the vertical seawall and the other considering the seawall defended by porous reef breakwater. Based on the two cases, the pressure reduction (P^*) due to the presence of the reef breakwater in tandem to the seawall is ascertained. In other words, P^* is the ratio of the hydrodynamic pressure realized in seawall due to the presence of reef breakwater in the seaside to that of the hydrodynamic pressure realized in seawall without reef breakwater. The pressure probes were located vertically along the face of the seawall till still water level (SWL). The pressure gauges were located at $z/d = 0$, (-)0.17, (-)0.33, (-)0.50, (-)0.67, (-)0.83. Where z is the point of interest and defined negative below SWL. The length of the pool (l_p) is considered to be a significant parameter (Madrigal and Homme 1991) in this context. Hence, the effects on pressure reduction on the seawall

due to change in pool length investigated in the study. The changes due to pool length is represented in nondimensional form as l_p/L, which is defined as relative pool length. The range of l_p/L studied in the present work is 0.47-1.4 as perceived in Table 2. In order to investigate the effects due to pool length, the lp was varied for the study whereas the relative water depth was kept constant (d/L =0.14). The wave heights were also varied in the study giving rise to a relative wave height range of 0.13-0.22.

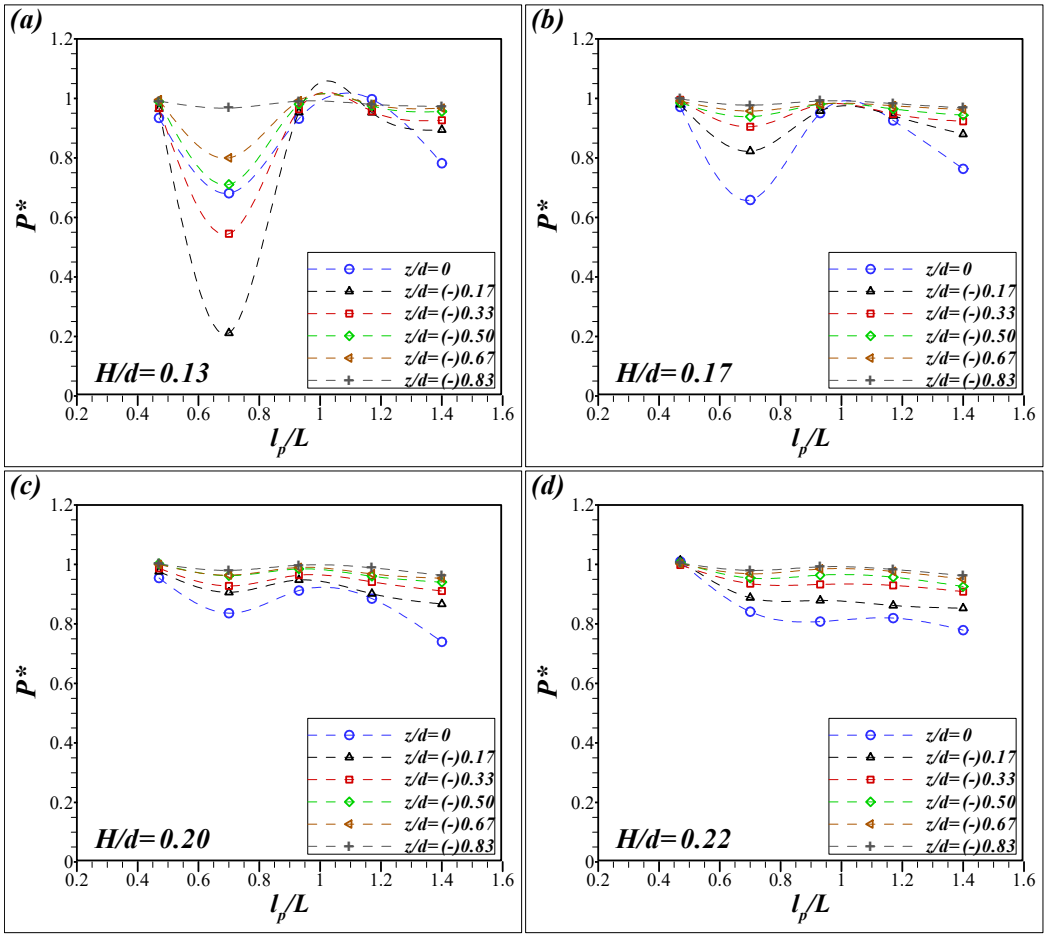

Figure 15: Effects of relative pool length (l_p/L) on the relative pressure (P^*) as a function of depth of pressure probe location, z/d. The results pertaining to H/d= 0.13, 0.17, 0.20 and 0.22 is portrayed in (a), (b), (c) and (d) respectively.

Figure 15 brings out the variations in pressure reduction, P^* as a function of relative pool length, l_p/L. Further, Figures 15(a), 15(b), 15(c) and 15(d) represent variations in P^* with reference to lp/L for different wave height ratios, H/d =0.13, 0.17, 0.20 and 0.22 respectively. The overall examination of Figure 15 brings out a non-monotonic trend in the pressure reduction when studied as a function of l_p/L. The results reaffirm the past observations (Dhinakaran et al., 2002, Sundar and Subba rao, 2002) pertaining to pressure measurements on coastal structures where this oscillatory trend was witnessed. Further, the changes in the pressure reduction seem to increase with a reduction in relative wave height

(H/d). This may be due to the fact that the increase in wave heights produces higher dynamic pressures in relation to the lower wave heights. The numerical simulations were performed with constant water depth (d) at the toe of the structure and hence changes in relative wave height (H/d) essentially mean the wave height variations. Additionally, the oscillatory behavior of the dynamic pressure is pronounced in the pressure probe close to SWL. This may be appreciated from Figure 15. This is expected as the extent of dynamic pressure is maximum at the free surface and decays below the SWL. Hence it may be argued here that the observations on the pressure reduction close to the SWL is of utmost importance. It can be perceived from Figure 15 that the pressure reduction is always less than unity under all the conditions considered in the study. This suggests that the effects of reef breakwater placed in tandem to the seawall have contributed to the reduction in hydrodynamic pressure.

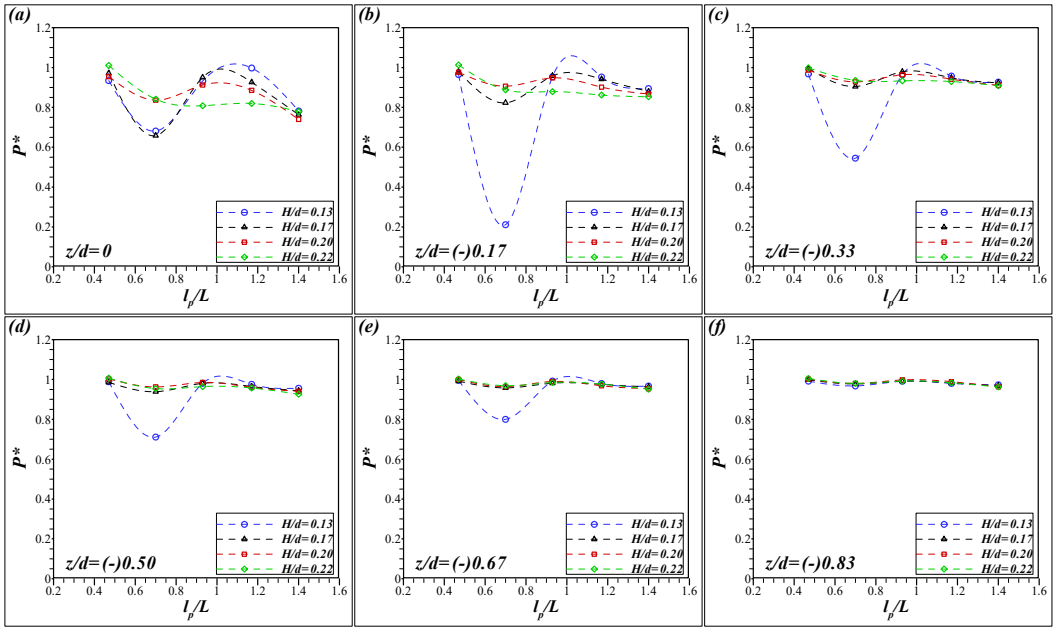

Figure 16: Effects of relative pool length (l_p/L) on the relative pressure (P^*) as a function of relative water depth (H/d). The results pertaining to z/d= 0, (-)0.17, (-)0.33, (-)0.50, (-)0.67 and (-)0.83 is described in (a), (b), (c), (d), (e) and (f) respectively.

In order to bring in the effects relative pool length (l_p/L) and relative wave height (H/d), the pressure reduction, P^* is depicted for constant z/d values. This can be witnessed from Fig 16. With such representation, the pronounced oscillatory behavior in pressure reduction can be noticed evidently in Figure 16(a) corresponding to z/d =0. Further, due to less dynamic pressure effects at the flume bed, one may not observe significant variations in the pressure reduction due to the placement of reef breakwater in tandem to the see was. This can be appreciated from Figure 16(f) which represents pressure reduction for z/d=(-)0.83. Further, the effects due to change in relative wave heights are not perceived from Figure 16(f) which gives a clear indication that the effects of the wave is less felt at the bottom. The oscillatory trend in the P^* at lower H/d values and its gradual reduction towards the flume bed can be appreciated from Figure 16(a)-(f). Though, it may be inferred that the oscillatory behavior

in pressure reduction is substantial at lower H/d (=0.13) and close to SWL, it is not complied in z/d =0 and H/d =0.13 which may due additional dissipation due to wave breaking effects as it falls close to d'/H =1.5 (Srineash and Murali 2019).

At the Still water Level (SWL), z/d =0, it is noticed that P^* takes values up to 0.68 which denotes about 32% reduction in pressure due to the presence of the porous structure in front of the seawall. There are no appreciable effects due to the presence of the porous structure at the pressure probe locations close to the flume bed, z/d =(-)0.83 (as P^* is close to 1 for the entire range of l_p/L). Further, for H/d =0.13 [Figure 15(a)], there is a relatively higher dip in pressure noted [Figures 16(b)-1(e)]. This is consistently noted across all z/d which depicts the oscillatory behavior in P^*. Further, the mean of pressure reduction at the free surface is noticed to be around 0.86 which represents 14% pressure reduction due to the presence of the reef breakwater placed in tandem to the seawall. The mean values of P^* across various H/d are 0.77, 0.91, 0.9, 0.75 and 0.97 for l_p/L = 1.4, 1.17, 0.93, 0.7 and 0.47 respectively at SWL [i.e., z/d =0]. These aspects suggest that there is still scope for research to examine the effects of reef parameters (B/d, d'/d) on pressure reduction on the structures on the lee side. For instance, one may expect an increase in pressure reduction, P^* with an increase in d' of the reef breakwater (Reddy and Neelamani 2004). Further, the effects of l_p/L may be examined for a wider range to identify the regions of l_p/L catering to lower P^*. A parametric study on the effects of reef parameters, wave parameters and its influence on pressure reduction on the structure leeside may be considered as future scope to address the challenges faced in reference to coastal engineering domain.

Typical snapshots showing velocity contours in the vicinity of the seawall defended by porous reef breakwater are brought out in Figures 17(a), 17(b), 17(c) and 17(d) for t/T =30.53, 30.78, 31.0 and 31.14. This case corresponds to a d/L of 0.14. The contours represent horizontal velocity (u_x) and a maximum velocity of about 0.47 m/s is realized in the study. The significance of the velocity contours and its engineering application is brought out in the earlier section of the manuscript. Figure 17(a) indicates the velocity contours when the wave approaches the reef. Wave interaction with the reef and its propagation over the crest of the structure can be witnessed from Figure 17(b) and 17(c). Further, the velocity contours pertaining to the transmitted wave is illustrated in Figure 17(d). On observing the velocity contours from Figure 17, it could be understood that the wave on interacting with reef breakwater gets transformed into multiple crests. This, in turn, enables wave attenuation which eventually reduces the wave pressures and loads on the structure on the leeside. This can be perceived from Figure 17 as the u_x values are always less than 0.2 m/s. Whereas, the velocity in the vicinity of the reef breakwater is as high as 0.47 m/s. This demonstrates the effectiveness of the reef breakwater in reducing the orbital velocities on the lee side and thereby reducing the magnitude of orbital velocity in front of the seawall.

4 Discussion

In this study, the wave interaction with submerged porous structure is examined with VRANS equations using open-source CFD code, REEF3D. The results from the numerical simulations are compared with the laboratory measurements involving varying configurations of the porous structure with different crest widths. The comparative study involved a comparison of experimental measurements with the numerical simulations for wave elevations and hydrodynamic

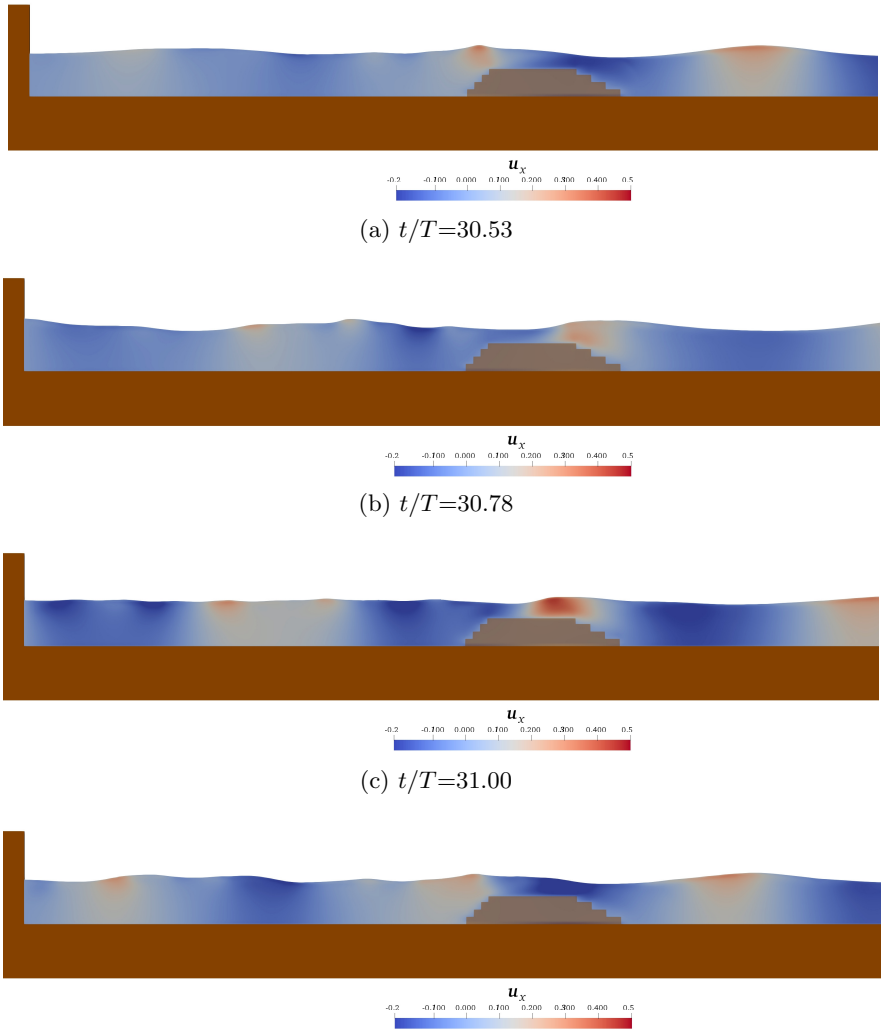

(a) t/T=30.53

(b) t/T=30.78

(c) t/T=31.00

(d) t/T=31.14

Figure 17: Velocity contours in the vicinity of seawall defensed by submerged porous reef breakwater [u_x in m/s].

pressures. Based on the present study, the values of the linear and nonlinear drag coefficients (α and β) is found to take the values of α=500 and β=3.3 for the porosity of 0.37 and D_{50} =0.01. Wave transmission characteristics of the porous structure modeled as a reef breakwater are also examined in the study along with wave decomposition and frequency analysis. The study demonstrates the ability of the CFD tool to perform coastal resilience studies. This has been performed by studying the pressure reduction on the seawall defended by a porous reef breakwater on its seaside. Such studies are beneficial to perform climate change mitigation studies in places where there is a need to strengthen the existing marine structures against the increased occurrence of severe wave conditions.

5 Conclusions

In the present study, it noticed that the numerical tool is able to reproduce the physical processes affecting the wave elevation. The simulations are able to replicate the effects of partial reflection in front of the porous structure appropriately. Further, the transmitted wave, past the submerged porous structure, is seen to undergo wave decomposition leading to dispersive tail waves and the model adopting VRANS approach was able to capture this effect similar to the experiments. The present numerical model is also able to reproduce the hydrodynamic pressures on the seaward, leeward and within the porous structure on par with the experiments. These aspects increase the confidence of adopting the VRANS approach for such wave structure interaction problems.

The numerical analysis was further extended to study the effect of crest width ($B = d$; $2d$ and $3d$) on wave attenuation for varying wave parameters. It is seen from the numerical study that wave attenuation increases with a decrease in relative depth of submergence (d'/H) and an increase in crest width ratio (B/d). Based on the investigations, it is found that the wave breaking induced due to the presence of the porous structure facilitates in achieving significant wave attenuation. The wave breaking process is also demonstrated with velocity contours in the study. A frequency- domain analysis is carried out to examine the energy distribution in the incident and transmitted spectra which revealed that the redistribution of energy to higher frequencies become prominent for transmitted wave spectrum with increase crest width and reduction in relative water depth d/L.

The open-source CFD, REEF3D combined with VRANS approach is seen to be a powerful tool to study the wave propagation over the porous structure. This has been verified for configurations involving various crest widths and the numerical model was able to reproduce the near structure flow properties appropriately. Further, the investigation is extended to study a potential solution to increased wave action on existing coastal protection structures due to climate change. This has been performed by studying the pressure reduction on a vertical seawall due to the introduction of a reef breakwater at the seaside.

Based on the study, it is perceived that the pressure reduction (P^*) due to the presence of porous structure in front of the seawall is always less than unity suggesting a reduction in hydrodynamic pressure due to the presence of porous structure. A pressure reduction up to 32% is calculated due to the presence of the porous structure in front of the seawall. This demonstrates the application of reef breakwaters for coastal resilience studies. The examination of the results suggests that there is an oscillatory trend observed in the pressure reduction, P^* when studied as a function of relative pool length, l_p/L. This oscillatory behavior in the pressure reduction, is noticed to increase with a reduction in relative wave height (H/d). Further, the hydrodynamic pressure is noticed to be maximum close to the free surface and tends to decay towards the flume bed. The study suggests that there is still scope for research to investigate the effects of reef and wave parameters on the pressure reduction on the leeside structure.

Acknowledgements

This study was supported in part with computational resources at the Norwegian University of Science and Technology (NTNU) provided by the Norwegian Metacenter for Computational

Science, NOTUR (No. NN2620K).

References

Aggarwal, A., Bihs, H., Shirinov, S., and Myrhaug, D., 2019. Estimation of breaking wave properties and their interaction with a jacket structure. Journal of Fluids and Structures, 91, 102722.

Ahmad, N., Bihs, H., Myrhaug, D., Kamath, A., and Arntsen, Ø. A., 2019. Numerical modeling of breaking wave induced seawall scour. Coastal Engineering, 150, 108-120.

Ahrens, J. P., 1984. Reef type breakwaters. Proc. of the 19th Coastal Eng. Conference, Houston, Tex., Sept., 2648-2662.

Ahrens, J. P., 1987. Characteristics of Reef Breakwaters, Technical Report CERC-87-17, U.S. Army Corps of Engineers, Waterways Experiment Station, Vicksburg.

Beji, S. and Battjes, J. A., 1993. Experimental investigation of wave propagation over a bar. Coastal Eng., 19(1–2), 151–162.

Bihs, H., Kamath, A., Alagan Chella, M., Arntsen, A., and Aggarwal, A., 2016a. A new level set numerical wave tank with improved density interpolation for complex wave hydrodynamics. Journal of Computers and Fluids, 140, 191–208.

Briganti, R., van der Meer, J.W., Buccino, M., Calabrese, M., 2003. Wave transmission behind low crested structures. Proceedings of Coastal Structures, Portland, Oregon. 580 - 592.

Dattatri, J., Sankar, N.J., Raman, H., 1978. Performance characteristics of submerged breakwaters. Proceedings of the 16th Coastal Engineering Conference, ASCE, (130), 2153–2171.

d'Angremond, K., van der Meer, J., and De Jong, R., 1996. Wave transmission at low-crested structures, Proceedings of the 25th Coastal Engineering Conference, ASCE, New York, 2418-2427.

Dhinakaran, G., Sundar, V., Sundaravadivelu, R., and Graw, K. U., 2002. Dynamic pressures and forces exerted on impermeable and seaside perforated semicircular breakwaters due to regular waves. Ocean Engineering, 29(15), 1981-2004.

Engsig-Karup, A. P., J. S. Hesthaven, H. B. Bingham, and T. Warburton., 2008. DG-FEM solution for nonlinear wave-structure interaction using Boussinesq-type equations. Coastal Engineering, 55 (3): 197–208.

Garcia, N., Lara, J., Losada, I., 2004. 2-D numerical analysis of near-field flow at low-crested permeable breakwaters. Coastal Engineering, 51, 991–1020.

Hall, K. R. and Seabrook, S. R., 1998. Design Equation for Transmission at Submerged Rubblemound Breakwaters. Journal of Coastal Research, 26, 102-106.

Higuera, P., Lara, J.L., Losada, I.J., 2013a. Realistic wave generation and active wave absorption for Navier–Stokes models. Coastal Engineering, 71, 102–118.

Higuera, P., Lara, J.L., Losada, I.J., 2013b. Simulating coastal engineering processes with OpenFOAM®. Coastal Engineering, 71, 119–134.

Jensen, B., Jacobsen, N., and Christensen, E., (2014). Investigations on the porous media equations and resistance coefficients for coastal structures. Coastal Engineering, 84, 56–72.

Johnson, J.W., Fuchs, R.A. and Morison, J.R., 1951. The damping action of submerged breakwaters. Transactions of American Geophysical Union, 32(5): 704-718.

Kamath, A., Alagan Chella, M., Bihs, H., and Arntsen, Ø. A., 2017. Energy transfer due to shoaling and decomposition of breaking and non-breaking waves over a submerged bar.

Engineering Applications of Computational Fluid Mechanics, 11(1), 450-466.
Kamath, A., Sasikumar, A., Bihs, H., 2018. Numerical study of wave interaction with a submerged porous breakwater in combination with a floating breakwater. Coastal Engineering Proceedings, 1(36), 38.
Koraim, A. S., Heikal, E. M., and Zaid, A. A., 2014. Hydrodynamic characteristics of porous seawall protected by submerged breakwater. Applied Ocean Research, 46, 1-14.
Lara, J., Garcia, N., Losada, I., 2006. RANS modelling applied to random wave interaction with submerged permeable structures. Coastal Engineering, 53, 395–417.
Lin, P. and Karunarathna, S. A. S. A., 2007. Numerical Study of Solitary Wave Interaction with Porous Breakwaters. Journal of Waterway, Port, Coastal, Ocean Engineering, 133 (5), 352-368.
Liu, P. L.-F., Lin, P., Chang, K.-A., and Sakakiyama, T., 1999. Numerical modeling of wave interaction with porous structures. Journal of Waterway, Port, Coastal, Ocean Engineering, 125(6), 322–330.
Losada, I, J., Lara, J, L., and Jesus, M, 2016. Modeling the Interaction of Water Waves with Porous Coastal Structures. Journal of Waterway, Port, Coastal, Ocean Engineering, 142 (6), 1- 18.
Madrigal, B. G. and Prud'Homme, J. O., 1991. Reduction of wave forces and overtopping by submerged structures in front of a vertical breakwater. In Coastal Engineering 1990 (pp. 1348-1361).
Miquel, A., Kamath, A., Alagan Chella, M., Archetti, R., and Bihs, H., 2018. Analysis of different methods for wave generation and absorption in a CFD-based numerical wave tank. Journal of Marine Science and Engineering, 6(2), 73.
Murali, K., 1996. Performance analysis of a cage floating breakwater. Chennai, India: Indian Institute of Technology Madras, Ph. D Thesis, 225p.
Ong, M. C., Kamath, A., Bihs, H., and Afzal, M. S., 2017. Numerical simulation of free-surface waves past two semi-submerged horizontal circular cylinders in tandem. Marine Structures, 52, 1-14.
Pilarczyk, K. W., 2003. Design of low-crested (submerged) structures: An overview. In 6th COPEDEC (International Conference on Coastal and Port Engineering in Developing Countries),(Srilanka), 1-19.
Reddy, M. M. and Neelamani, S., 2005. Hydrodynamic studies on vertical seawall defenced by low-crested breakwater. Ocean Engineering, 32(5-6), 747-764.
Sasikumar, A., Kamath, A., Musch, O., Bihs H., and Arntsen, A., 2018. Numerical study on the effect of a submerged breakwater seaward of an existing breakwater for climate change adaptation. Proceedings of OMAE 2018, 77965, 1-10.
Sasikumar, A., Kamath, A., Musch, O., Bihs, H., and Arntsen, Ø. A., 2019. Numerical Modeling of Berm Breakwater Optimization with Varying Berm Geometry Using REEF3D. Journal of Offshore Mechanics and Arctic Engineering, 141(1), 011801.
Schäffer, H. and Klopman, G., 2000. Review of multidirectional active wave absorption methods. Journal of Waterway, Port, Coastal, Ocean Engineering, 2(88),88–97.
Seabrook, S. and Hall, K., 1998. Wave transmission at submerged rubble-mound breakwaters, Proceedings 26th Coastal Engineering Conference, ASCE, 2000 - 2013.
Srineash, V. K. and Murali, K., 2015. Hydrodynamic Performance of Gabion Box Artificial Reefs, Proceedings of the 25th International Ocean and Polar Engineering Conference (ISOPE), (Hawaii, USA), 1438-1442.

Srineash, V. K. and Murali, K., 2018. Wave Shoaling over a Submerged Ramp: An Experimental and Numerical Study. Journal of Waterway, Port, Coastal, Ocean Engineering, 144 (2), 04017048-1-12.
Srineash V. K. and Murali K., 2019. Functional performance of modular porous reef breakwaters. Journal of Hydro-environment research, 27, 20-31. doi:10.1016/j.jher.2019.07.006
Sundar, V. and Subba rao, B. V. V., 2002. Hydrodynamic pressures and forces on quadrant front face pile supported breakwater. Ocean engineering, 29(2), 193-214.
Tanaka, N., 1976. Effects of submerged rubble-mound breakwater on wave attenuation and shoreline stabilization. Proc., Japanese Coastal Engineering Conference, JSCE, Tokyo, 152–157 (in Japanese).
Troch, P., 2000, Experimentele Studie En Numerieke Modellering Van Golf interactie Met Stortsteen golfbrekers. Ghent, Belgium: Ghent University, Ph.D. dissertation.
Van der Meer, J.W., Daemen, I.F.R., 1994. Stability and wave transmission at low crested rubble mound structures, Journal of Waterway, Port, Coastal, Ocean Engineering, 1, 1–19.
Van Gent, M.R.A., 1995. Porous flow through rubble-mound material. Journal of Waterway, Port, Coastal, Ocean Engineering, 121, 176–181.
Van der Meer, J.W., Briganti, R., Zanuttigh, B., Wang, B., 2005. Wave transmission and reflection at low crested structures: design formulae, oblique wave attack and spectral change. Coastal Engineering, 52.
Zhang, S. X. and Li, X., 2014. Design formulas of transmission coefficients for permeable breakwaters. Water Science and Engineering, 7(4), 457-467.